A Full-Duplex Single-Chip Transceiver With Self-Interference Cancellation in 0.13 μm SiGe BiCMOS for Electron Paramagnetic Resonance Spectroscopy

Xuebei Yang and Aydin Babakhani

***Abstract*— This paper presents a miniaturized EPR spectrometer based on a single-chip transceiver. Utilizing a novel on-chip self-interference cancellation circuit, the electromagnetic coupling from the transmitter (TX) to the receiver (RX) is minimized, allowing simultaneous achievement of large TX output power and low RX noise figure (NF). In the measurement, the RX achieves a NF of 3.1 dB/6.3 dB at 10 MHz/50 kHz baseband frequencies, when the TX and cancellation circuits are turned off. The measured flicker noise corner is 60 kHz, more than 10× lower than the prior work. Moreover, for the first time, the operation of the RX and cancellation circuit is demonstrated when a co-integrated TX is operating at the same time and frequency, while producing >20 dBm output power. When the TX and cancellation circuits are turned on, at −10 dBm interference power, the measured NF is 6.8 dB/11.1 dB at 10 MHz/50 kHz baseband frequencies. This is lower by 5.6 dB/9.6 dB at 10 MHz/50 kHz baseband frequencies, compared to the NF with the cancellation circuit off at the same interference power. The transceiver chip is implemented in IBM 0.13 μm BiCMOS process and consumes a power of 2 W. Utilizing this transceiver, an electron paramagnetic resonance (EPR) spectrometer is built and tested. It is observed, through measurement, that the interference cancellation circuit increases the signal-to-noise ratio (SNR) of the EPR signal by 7 dB at −10 dBm interference power. Compared to prior work, the reported EPR spectrometer improves the sensitivity of the system by 25 dB.**

***Index Terms*— BiCMOS, electron paramagnetic resonance, electron spin resonance, full-duplex, self-interference cancellation, SiGe, silicon, transceiver.**

I. Introduction

THE electron paramagnetic resonance (EPR) phenomenon is based on the interaction of an electron magnetic dipole with an electromagnetic field, in the presence of a DC magnetic field. Since the first observation in the mid-1940s [1], EPR spectroscopy has found its application in numerous fields. In clinical medicine, EPR spectroscopy is the only direct and non-invasive method that can monitor the partial oxygen pressure (pO_2) in human vessels and tissues. This measurement provides vital information in the treatment of cardiovascular diseases and during the radiation therapy [2]–[4]. In the oil and gas industry, EPR spectroscopy is used to determine the concentration of various paramagnetic chemicals in crude oil, such as asphaltenes, corrosion ions, and vanadyl complexes VO^{2+} [5], [6]. In the semiconductor industry, EPR spectroscopy provides a powerful tool for detecting point defects in semiconductor lattices, including silicon, silicon carbide, zinc oxide [7], [8].

Unfortunately, while EPR spectroscopy has demonstrated its significance in various fields, this technique has only been exploited in few research laboratories. This is caused primarily by the deficiencies of existing commercial EPR spectrometers. Traditionally, an EPR spectrometer consists of a large number of discrete electrical components, which are usually built with dedicated and expensive processes. As a result, the cost, weight, and size of traditional EPR spectrometers are prohibitively large, restricting their use in hand-held applications [22].

In order to reduce the cost, weight, and size of EPR spectrometers, recent efforts have focused on integrating the electrical components of the EPR spectrometer through the use of silicon integrated-circuit technology [9]–[11]. For example, in [11] the RF transceiver of an EPR spectrometer was integrated onto a single chip, which represents the highest level of integration so far. However, the EPR spectrometer reported in [11] suffered from relatively low sensitivity, mostly due to a TX self-interference problem. In order to mitigate the TX self-interference problem, in [11] the TX power was deliberately lowered to about 5 dBm. Unfortunately, existing studies have shown that the EPR signal power generated by the sample is proportional to the TX power sent to the sample [12]. Therefore, the EPR spectrometer reported in [11] has a relatively poor sensitivity.

In this paper, we propose a technique to enhance the sensitivity of the EPR spectrometer by mitigating the TX self-interference. Although TX self-interference is a rather general problem that would appear in all in-band full-duplex applications, the unique operating condition of EPR spectroscopy poses specific challenges to the transceiver. In EPR spectroscopy, the TX interference is an unmodulated continuous-wave signal, which to some extent, relaxes the linearity and intermodulation requirement for the RX. However, the frequency of the baseband signal is typically lower than 100 kHz, which poses stringent requirement to the RX noise figure (NF)

Manuscript received March 20, 2016; revised May 17, 2016 and July 6, 2016; accepted July 8, 2016. Date of publication August 18, 2016; date of current version September 30, 2016. This paper was approved by Associate Editor Pietro Andreani.

The authors are with Rice University, Houston, TX 77005 USA.

Color versions of one or more of the figures in this paper are available online at http://ieeexplore.ieee.org.

Digital Object Identifier 10.1109/JSSC.2016.2592998

at low baseband frequencies. In prior in-band full-duplex transceivers [13]–[17] that targeted wireless communication applications, mixer-first or current-mode mixer-first architectures were mostly utilized. These architectures unfortunately resulted in a poor RX NF especially at low baseband frequencies. As a result, TX interference-resilient techniques based on mixer-first architectures cannot be directly applied in EPR spectroscopy. Furthermore, in prior interference-resilient-transceiver papers, the TX is either not implemented on the same chip, or is integrated on the same chip but remains off during RX measurements. Therefore, the true performance of the RX remains unknown when a co-integrated TX is on and operating at the same frequency band as the RX. One exception is [13], where the RX was measured while a co-integrated TX was simultaneously operating. However, the TX in [13] was only generating a weak output power around -18 dBm during the measurement.

In this work, we report a single-chip in-band full-duplex transceiver for EPR spectroscopy, where TX power is targeted at >20 dBm while RX is operating at the same time and frequency band. In this design, the TX self-interference problem is mitigated by an on-chip cancellation circuit. This improves RX performance through canceling the TX self-interference by at least 32 dB. For the first time, operation of a self-interference-resilient RX is demonstrated while a co-integrated TX is operating and generating >20 dBm output power. Moreover, low NF at low baseband frequencies is achieved. When the TX and self-interference cancellation circuits are turned off, the RX achieves a measured NF of 3.1 dB/6.3 dB at 10 MHz/50 kHz baseband frequency, with a 60 kHz flicker noise corner. This flicker noise corner is more than $10\times$ lower than the prior publications [15], [16]. At -10 dBm self-interference power, the measured RX NF is 6.8 dB/11.1 dB at 10 MHz/50 kHz baseband frequency when the self-interference cancellation circuit is turned on. The NF increases by 5.6 dB/9.6 dB at 10 MHz/50 kHz baseband frequency when the self-interference cancellation circuit is turned off, demonstrating the functionality and importance of the self-interference cancellation circuit. Utilizing this transceiver, an EPR spectrometer is assembled and characterized by measuring a 2,2-Diphenyl-1-Picrylhydrazyl (DPPH) powder sample. At -10 dBm self-interference power at the input of the RX, the SNR of the EPR signal improves by 7 dB when the cancellation circuit is turned on. Compared to the previous work presented in [11], the reported EPR spectrometer shows a SNR improvement of 25 dB.

The paper is outlined as follows. Section II discusses the background of EPR spectrometers and the importance of the self-interference cancellation. Section III describes the design of the single-chip transceiver with self-interference cancellation circuit. Section IV reports the measurement results of the transceiver, as well as the assembled spectrometer, and Section V concludes the paper.

II. Background

In this section, the background of EPR spectroscopy is first introduced. Next, the importance of self-interference cancellation is discussed.

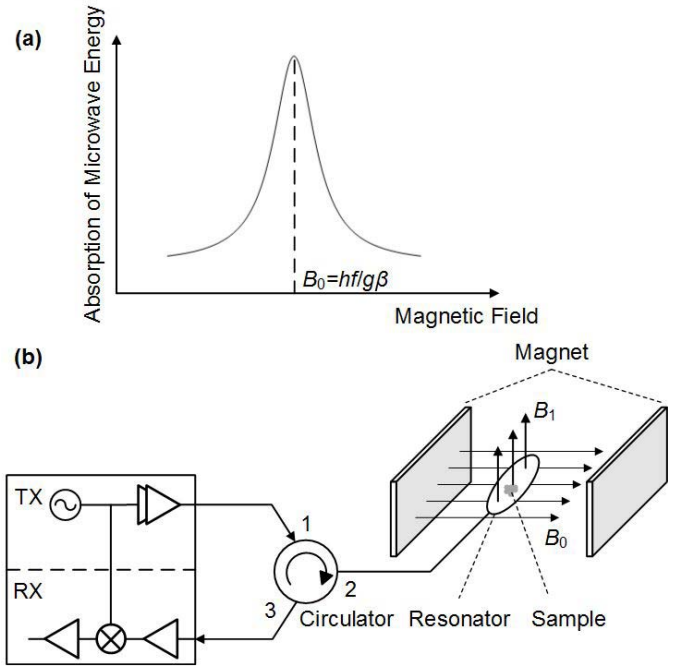

Fig. 1. (a) Energy absorption of an EPR sample versus DC magnetic field. (b) Architecture of a typical continuous-wave absorption-power-based EPR spectrometer.

A. EPR and EPR Spectrometer

From the quantum physics theory, it is known that electrons with spin quantum number M_s possess a magnetic moment of $g\beta M_s$. Here, g is a material-dependent constant, and β is equal to $9.2740154 \times 10^{-24}$ JT^{-1}. When an electron is placed inside a magnetic field B_0, it obtains an energy of $U = B_0 g\beta M_s$. For a spin 1/2 system where possible values for M_s are $+1/2$ and $-1/2$, there exist two possible electron spin energy levels, and the energy difference between the two energy levels is equal to $\Delta U = B_0 g\beta$. In materials where empty electron spin energy levels exist, an electron transition from the lower energy level to the higher energy level may be induced by an electromagnetic field B_1 with appropriate frequency f, where the photon energy satisfies $hf = \Delta U = B_0 g\beta$. The frequency f typically falls into the microwave regime. In reality, due to effects such as the interaction between electrons with nearby electrons and lattice, for a given microwave frequency f, the absorption of energy may occur across a range of magnetic field centered around B_0, as shown in Fig. 1(a). This phenomenon, that certain materials, when placed inside a magnetic field, will absorb incoming microwave energy at a particular frequency, is called Electron Paramagnetic Resonance (EPR).

In order to measure the absorption curve of a sample shown in Fig. 1(a), typically an EPR spectrometer is used. In this work, we focus on continuous-wave absorption-power-based EPR spectrometer, as it is the most widely-used EPR spectrometer. Fig. 1(b) shows the architecture of an absorption-power-based EPR spectrometer. During the measurement, the TX delivers a microwave signal to the resonator, which contains the sample. The resonator generates a strong

electromagnetic field B_1, which interacts with the sample and excites electron transition. The amplitude of the magnetic field B_0 is gradually swept, but the frequency and power of the TX signal is fixed. The RX receives the reflected power from the resonator, which varies when the sample absorbs part of the microwave signal inside the resonator. This absorption depends on the DC magnetic field inside the resonator and reaches a maximum value as shown in Fig. 1(a). Since this absorption is small, it is difficult to measure the change in the reflected signal coupled to the receiver. This is because the change results in a small DC signal after down-conversion. To increase the sensitivity of the detection and reduce the effects of low-frequency noise ($1/f$), a small amplitude-modulated magnetic field (e.g., 0.1 Gauss) is applied on top of a large DC magnetic field by injecting a low-frequency AC current (e.g., 100 kHz) to the magnet coil. This technique shifts the baseband signal from DC to the modulation frequency (e.g., 100 kHz). In addition, the modulation mechanism converts the EPR curve, the amplitude of the base-band signal versus the DC field B_0, to a first-order derivative of the absorption line shown in Fig. 1(a). Theoretically, to maximize the sensitivity of the system, the modulation frequency should be much higher than the flicker noise corner of the RX. Unfortunately, due to limitations such as the difficulty of generating a strong high-frequency magnetic field, the modulation frequency in a typical EPR spectrometer rarely exceeds 100 kHz. This poses a stringent requirement on the RX NF at low baseband frequencies.

B. Background on TX Self-Interference

In an absorption-power-based EPR spectrometer, the minimally-detectable number of electron spins is equal to

$$\left(\frac{4k_B}{g^2\beta^2\mu_0}V_s\mathrm{T}\right)\left(\frac{\Delta\omega}{\omega_0}\right)\left(\frac{1}{Q\eta}\right)\sqrt{\frac{Fk_BT}{P}} \tag{1}$$

where V_s and T are the volume and temperature of the sample, respectively. k_B is the Boltzmann constant. μ_0 is the vacuum permeability. $\Delta\omega$ is the spectral line width of the sample, which is a material-dependent constant. η and Q are the filling factor and quality factor of the resonator, respectively. ω_0 is the operational frequency of the EPR spectrometer. F is the noise factor of the RX, and P is the TX output power [12]. The equation is derived by comparing the EPR signal power of the sample and the noise power of the RX, and the minimally detectable number of electron spins is defined when these two powers are equal (SNR $=$ 1). Clearly, the RX NF should be reduced and the TX output power should be maximized. Note that the equation above has not included the sample saturation effect, where the EPR signal power of the sample may stop to increase if the TX power exceeds the sample saturation power. Existing studies have shown that the sample saturation power is strongly sample-dependent and can be as large as several tens of milliwatts [18]. Therefore, in this work, the maximum TX output power is targeted at around 20 dBm. Unfortunately, for this amount of TX output power, it is difficult to achieve low RX NF using prior single-chip-transceiver-based EPR spectrometers [11]. This is caused by the TX self-interference signal present at the RX input. During the operation of an EPR spectrometer, a small portion of the TX signal, denoted as TX self-interference, always couples to the RX input through two major coupling mechanisms: 1) the finite isolation value of the circulator, and 2) the reflection from the resonator due to non-perfect matching. As a commercial circulator typically does not provide an isolation of better than 30 dB, the TX self-interference signal is about 30 dB lower than the TX output power. The frequency of the self-interference signal only deviates from the RX frequency by the modulation frequency of the B_0 field, which is no more than 100 kHz. Because the frequency of the TX self-interference and EPR signals deviate by such a small amount, it is extremely challenging to remove the TX self-interference signal before down-conversion by a filter. As indicated before, the baseband frequency for an EPR spectrometer is same as the modulation frequency of the magnetic field B_0. In such low frequencies, the flicker noise of mixers and baseband amplifiers can contribute significantly to the RX NF, if it is not suppressed by a strong amplification before down-conversion. However, if the TX is generating a strong output signal, the TX self-interference would be excessively large at the RX input, saturating the RX and preventing a large signal gain. As a result, a large TX output power and a low RX NF cannot be simultaneously achieved without using a novel architecture. For example, the transceiver in [11] achieved a good RX NF at the cost of a relatively low TX output power of around 5 dBm. This limitation significantly impacted the sensitivity of the spectrometer.

In recent years, several techniques have been proposed that could mitigate the TX self-interference in an in-band full-duplex transceiver [13]–[17] that targeted at wireless communication applications. However, as described in the introduction section, these works provide poor NF at low baseband frequencies (for example, the flicker noise corner was 2 MHz in [15]), and thus they are not suitable for EPR spectroscopy.

III. Architecture of the Transceiver With TX Self-Interference Cancellation

In this work, in order to improve the sensitivity of the EPR spectrometer, we mitigate the TX self-interference by integrating a cancellation circuit on the transceiver chip. In this section, we first introduce the architecture of the transceiver. Next, the details of the self-interference cancellation circuit, TX, and RX are discussed.

A. Transceiver Architecture

As shown in (1), the sensitivity of an EPR spectrometer increases with the operation frequency. Therefore, it is attractive if the frequency can be maximized. However, in this work, a planar PCB-based resonator is used to minimize the cost and form factor of the spectrometer, and make it suitable for planar applications. Therefore, due to the challenges of fabricating a large planar high-Q resonator at high frequencies, the frequency of the prototype transceiver is designed to be around 4.5 GHz.

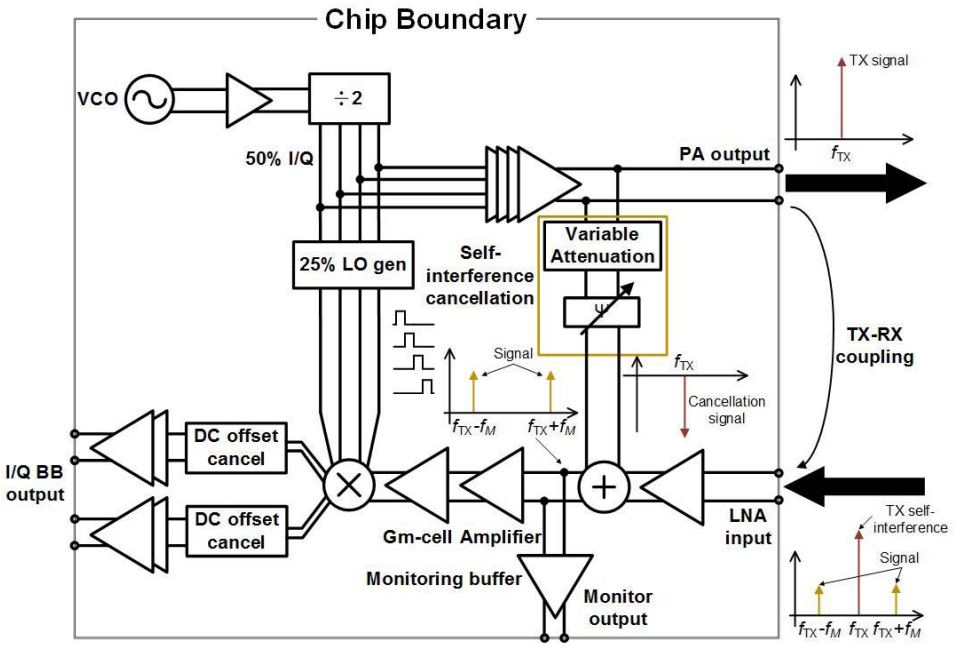

Fig. 2. Architecture of the reported transceiver.

The architecture of the proposed transceiver is presented in Fig. 2. In order to cancel the TX self-interference signal, an on-chip self-interference cancellation circuit is inserted between the TX and RX. The cancellation circuit takes the TX output as its input and then generates a cancellation signal with the same amplitude but a 180 phase shift, relative to the TX self-interference signal at the input of the receiver. In order to achieve a low RX NF, the noise penalty from the self-interference cancellation circuit must be minimized. Toward this purpose, the cancellation signal is injected after the low-noise amplifier (LNA), instead of at the RX input. By carefully choosing the gain of the LNA, the noise contribution from the cancellation circuit can be suppressed, while the RX still maintains good linearity.

After the TX self-interference signal is removed from the RX, the desired EPR signal is further amplified and then down-converted to baseband. At the baseband input, a DC offset filtering block is used to reject the DC offset. Because the baseband signal in EPR spectroscopy is typically on the order of tens of kHz, external 10μF capacitors are utilized in the DC offset filtering block. They can potentially be removed by implementing on-chip DC offset cancellation circuitries such as the one reported in [19]. After filtering, the remaining EPR signal is further amplified by baseband amplifiers and delivered to an off-chip data-acquisition unit for processing.

B. Self-Interference Cancellation Circuit

The self-interference cancellation circuit must generate a cancellation signal with tunable phase and amplitude to cancel the interference signal. In this work, no assumption is made on the phase of the interference signal, so the cancellation circuit is required to have 360° phase tunability. The amplitude of the TX self-interference signal is assumed to have a maximum value of approximately -10 dBm, considering 20 dBm TX output power and 30 dB TX-RX isolation. As introduced before, the cancellation signal is injected into RX after the EPR signal has been amplified by a LNA, whose gain is designed to be approximately 10 dB in this work; therefore, the maximum amplitude of the cancellation signal is required to exceed 0 dBm. Moreover, as the RX input-referred P1dB is estimated to be -25 dBm, it is desirable that the cancellation signal can have at least 15 dB of amplitude tunability so that a self-interference signal as high as -10 dBm can be cancelled as well. Fortunately, since the self-interference is a single-tone signal, the linearity requirement for the cancellation circuit is relatively relaxed, as no intermodulation signal with frequency close to the EPR signal will be generated.

Fig. 3 presents the schematic of the self-interference cancellation circuit. Because the TX output exceeds 20 dBm, it must be attenuated before being sent to the input of the cancellation circuit; otherwise, the active devices in the cancellation circuit may face severe reliability/breakdown concerns. As shown in Fig. 3, the attenuator at the input of the cancellation circuit is realized through a voltage divider. In order to reduce the noise from the self-interference cancellation circuit, we have merged the amplitude tuner with the attenuator instead of adding an extra stage to perform amplitude tuning for the cancellation signal. In this work, instead of a resistor divider, two reverse-biased diode varactors are used to perform the amplitude tuning to minimize the added thermal noise. By changing the capacitance of the varactors, the dividing ratio is varied. In a divider containing only two capacitors C_1 and C_2, as shown in Fig. 4 (a), if the varactor capacitance C_1 can be increased by N×, without considering the load impedance, the amplitude tuning range of the divider output is

$$\frac{NC_1 + C_2}{C_1 + C_2} \tag{2}$$

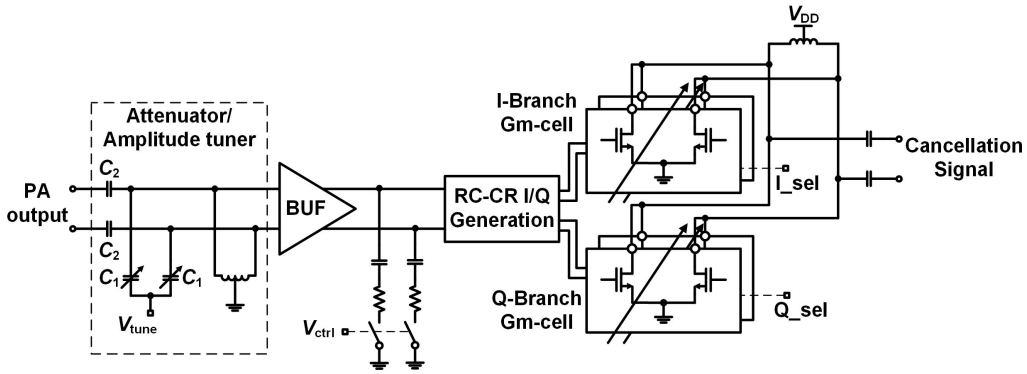

Fig. 3. Schematic of the self-interference cancellation circuit.

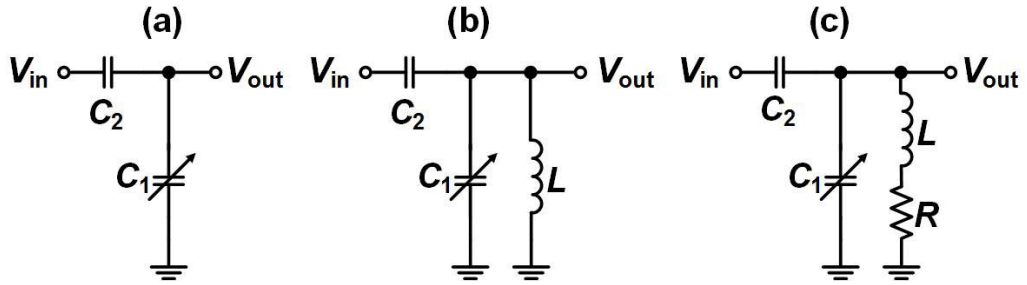

Fig. 4. (a) A simple capacitor divider. (b) Inductor-assisted capacitor divider with an ideal inductor. (c) Inductor-assisted capacitor divider with a real inductor.

To achieve a large amplitude tuning range at the divider output, the tuning range of the varactor capacitance should be maximized. Unfortunately, in the process where the proposed transceiver is implemented, the tuning range of the varactor capacitance is limited to approximately 2–3×. Therefore, the amplitude tunability of the divider output is restricted to 10 dB or less. This number could be further reduced if the load impedance is considered. In order to enlarge the amplitude tuning range of the divider output, in this work, a parallel LC resonance network is used to increase the tuning range for the effective capacitance of the varactor. As shown in Fig. 4(b), if an inductor is connected in parallel to the varactor, the admittance of the network becomes

$$Y = j\omega C_1 + \frac{1}{j\omega L} \tag{3}$$

If the value of L and C_1 are chosen such that the admittance always has a positive imaginary part, the effective capacitance of this LC network would be

$$C_{eff} = C_1 - \frac{1}{\omega^2 L} \tag{4}$$

Now the tuning range of C_{eff} is

$$\frac{NC_1 - \frac{1}{\omega^2 L}}{C_1 - \frac{1}{\omega^2 L}} \tag{5}$$

By choosing C_1 slightly larger than $\frac{1}{\omega^2 L}$, the tuning range of C_{eff} could be much larger than 3, and thus the amplitude of the divider output could achieve a large tuning range. Moreover, because the admittance of the LC network is purely imaginary and remains positive, the phase shift of the voltage divider is constant across all the dividing ratios.

In reality, the quality factor of the inductor may limit the amplitude tuning range of the divider output. If the inductor has a quality factor of Q, the admittance of the parallel LC network becomes

$$\begin{aligned} Y &= j\omega C_1 + \frac{1}{j\omega L + \frac{\omega L}{Q}} \\ &= j\omega C_1 - \frac{j\omega L}{\omega^2 L^2 \left(1 + \frac{1}{Q^2}\right)} + \frac{\frac{\omega L}{Q}}{\omega^2 L^2 \left(1 + \frac{1}{Q^2}\right)} \\ &\approx j\omega C_1 - \frac{j}{\omega L} + \frac{1}{\omega L Q} \end{aligned} \tag{6}$$

Note that the effective capacitance remains the same, as in the case where the inductor is ideal, but the admittance now has a positive real part. The resulting tuning range of the dividing ratio is

$$\frac{1 + j\omega^2 L Q(C_2 + C_{eff-max})}{1 + j\omega^2 L Q(C_2 + C_{eff-min})} \tag{7}$$

Here $C_{\text{eff-max}}$ and $C_{\text{eff-min}}$ are the maximum and minimum values of C_{eff}. This equation shows that, for the same values of C_{eff} and C_2, a lower inductor Q results in a lower tuning range of the dividing ratio. Moreover, the phase shift of the divider output would vary at different dividing ratios due to the finite inductor Q. Fig. 5 plots the simulated output of the voltage divider under different inductor Q. The simulation is performed at 4.5 GHz. C_2 is set at 200 fF, the inductance is chosen to be 0.8 nH, and C_1 is varied from 2 pF to 5 pF. As shown in the figure, the inductor Q should be maximized to

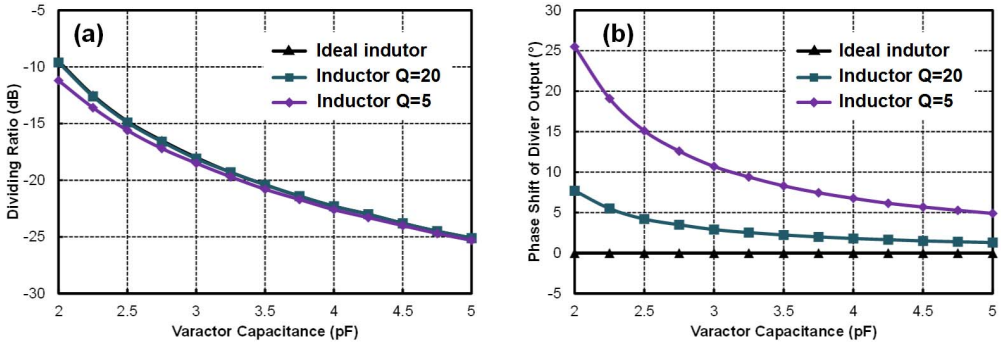

Fig. 5. (a) Simulation results for the dividing ratio under different inductor Q. (b) Simulation results for the phase shift of the divider output under different inductor Q.

achieve a large tuning range for the divider ratio and maintain a small variation in the phase shift of the divider output. In this work, with an inductor Q of 13, the divider output has a tuning range of 14 dB, and the phase shift across the entire tuning range is within 4 in the simulation.

In this work, a high input-impedance buffer follows the divider. The input impedance of the buffer can be absorbed into the quality factor of the inductor when analyzing the performance of the voltage divider. Because the amplitude of the divider output can still be large, high breakdown transistors are used when constructing the buffer. The load impedance of the buffer is designed to be variable so that 4 dB additional tuning of the amplitude of the cancellation signal can be achieved. An I-Q generator follows the buffer and converts the differential signal into quadrature. The quadrature signal is sent to a Cartesian phase shifter, which assigns different weights to the I and Q branches of the signal, and then combines them. The weights of the I and Q signals are controlled by varying the gain of the two buffers that amplify the signal. The cancellation is finally injected into the RX through a buffer.

One of the most important criteria of the self-interference cancellation circuit is that its noise contribution must be small. To achieve this goal, voltage amplification in the cancellation circuit is mostly avoided, as any voltage gain will amplify the noise of the cancellation circuit as well. Fig. 6 presents the simulation results of the noise contribution from the cancellation circuit. The simulation is performed when the gain of the cancellation circuit is set at the maximum value. At the LNA output, where the cancellation signal is injected to the RX, the noise from the cancellation circuit is much smaller than the noise caused by the LNA (including the noise from the 50Ω LNA input and the noise produced by the LNA). This translates to a noise figure penalty of only 0.2 dB.

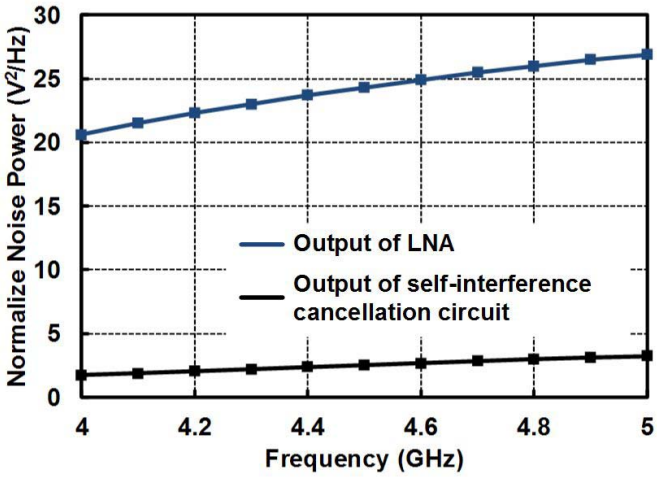

Fig. 6. Simulated noise power at the LNA output and the cancellation circuit output when the cancellation circuit gain is set at the maximum value. The self-interference cancellation circuit introduces a simulated noise figure penalty of only 0.2 dB.

C. Design of the TX and RX

In this section, the design of the TX and RX of the transceiver chip is presented.

In this work, the TX signal is generated using a voltage-controlled oscillator (VCO). The frequency of the VCO is designed to be twice the operation frequency of the EPR spectrometer. A frequency divider then divides the frequency of the VCO signal by two, simultaneously providing I and Q signals that are necessary to generate the LO signals for the down-conversion mixer. Fig. 7 presents the schematic of the VCO and the frequency divider. The VCO takes a differential cross-coupled design. As the VCO frequency is around 9 GHz, the frequency divider uses a current-mode logic (CML) structure, which is suitable for high-speed operation.

Following the frequency divider, an amplifier chain amplifies the TX signal. A power amplifier (PA) finally delivers the signal to a 50Ω off-chip load through an external balun. The schematic of the PA is shown in Fig. 8. The PA is based on a class-AB design and is fully integrated on the same chip. The simulated single-ended output-referred 1 dB compression point is 20 dBm.

The design of the RX front-end is presented in Fig. 9. The first stage in the RX is an inductive-degenerated cascode LNA. The load of the LNA is shared with the buffer of the self-interference cancellation circuit, which injects the cancellation signal at the LNA output. In order to monitor the effects of self-interference cancellation, a voltage-monitoring buffer is added at the LNA output. This buffer senses the LNA

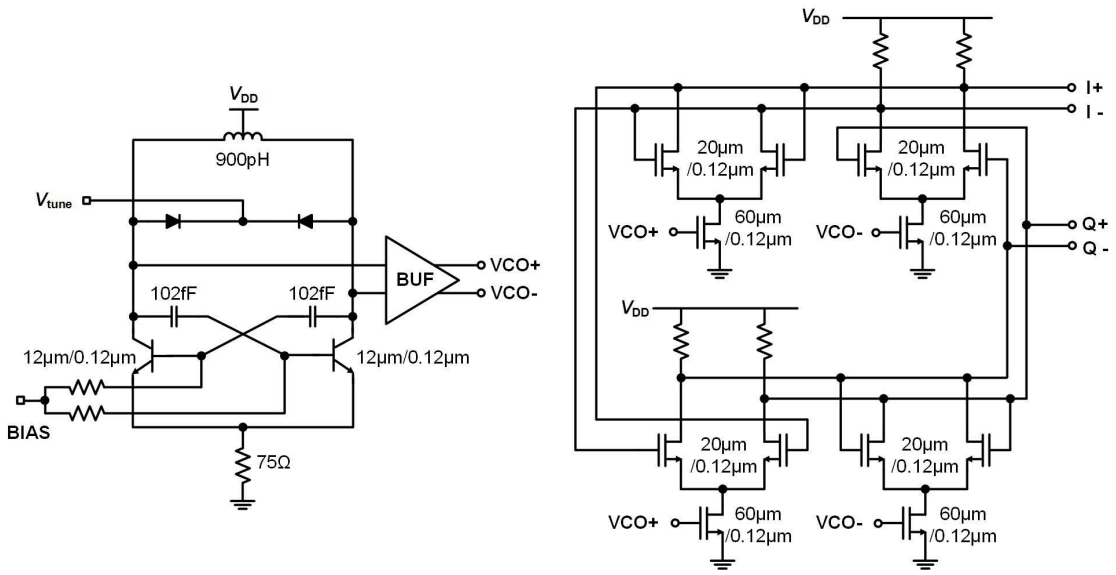

Fig. 7. Schematic of the VCO and the CML frequency divider.

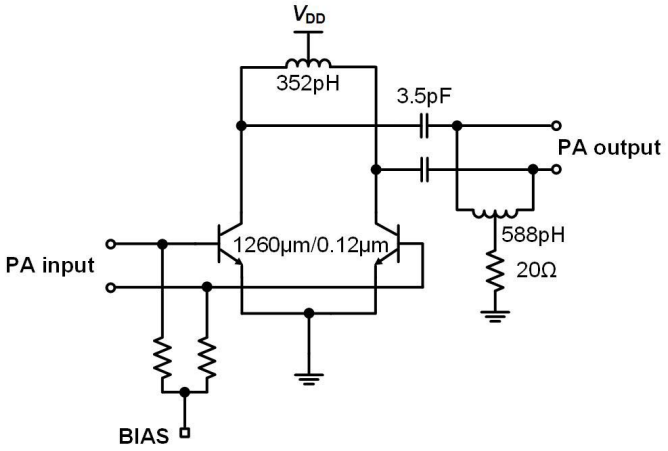

Fig. 8. Schematic of the PA.

output, attenuates it by 10 dB, and then sends it to output pads. The output of the monitoring buffer is used to guide the amplitude and phase tuning of the cancellation signal. After the TX self-interference signal has been removed from the RX, the remaining EPR signal is further amplified to suppress the flicker noise caused by mixers and baseband amplifiers. In this work, the down-conversion is performed by a current-mode passive mixer. Compared to active mixers, the passive mixer introduces a smaller flicker noise. Moreover, by minimizing the input impedance of the baseband trans-impedance amplifier (TIA), a current-mode passive mixer provides an improved linearity. This is because the large voltage swing, which causes device nonlinearities, is avoided in the circuit. The LO signal of the passive mixer is generated from the I/Q outputs of the frequency divider following the VCO. The signal has a 25% duty cycle, increasing the mixer conversion gain by 3 dB, compared to a 50% duty cycle LO [20]. The design of the G_m cell is also shown in Fig. 9. This block is constructed using a class-AB CMOS cell. As discussed in [21], such G_m cell has very high linearity. In simulation, the trans-conductance gain is only reduced by 1 dB when the single-ended input voltage swing reaches 1.4 V.

The design of the baseband amplifiers is shown in Fig. 10. The baseband TIA is implemented using a common-base amplifier. The input impedance is kept small, at 10Ω, to increase the linearity of the G_m cell and the passive mixer. The signal is finally amplified and delivered off-chip through a 50Ω buffer.

IV. Measurement Results

In this section, we first report the measurement results of the integrated transceiver, and then present the measured EPR response of various samples.

A. Transceiver Measurement Results

Fig. 11 shows the micrograph of the reported transceiver. The transceiver chip is fabricated in IBM 0.13 μm BiCMOS process technology. It occupies an area of 4.8 mm$\times$ 2.5 mm and consumes 2 W of DC power during the operation. Major blocks of the transceiver are labeled in the figure.

The measured frequency tunability of the TX signal is shown in Fig. 12. During this measurement, the voltage of the tuning node of the on-chip VCO is varied, and the frequency of the frequency divider output is measured using an Agilent signal analyzer N9030A. As shown in the figure, the frequency of the signal can be varied from 3.8 GHz to 5.2 GHz.

The TX output power versus frequency is shown in Fig. 13. This power is measured after the differential TX outputs have been combined using an off-chip balun. It is observed that the TX can generate a maximum output power of 22 dBm. The measured 3 dB bandwidth is 1 GHz (from 3.8 to 4.8 GHz.)

The performance of the self-interference cancellation circuit is shown in Fig. 14. The purpose of this measurement is to

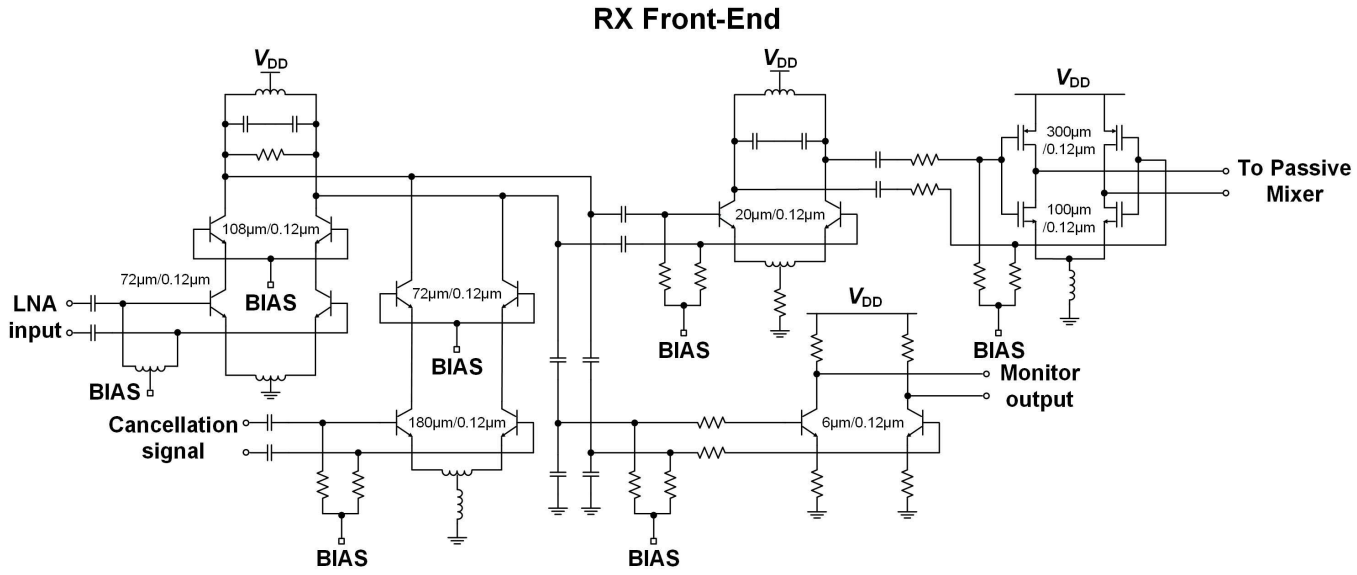

Fig. 9. Schematic of the RX front-end.

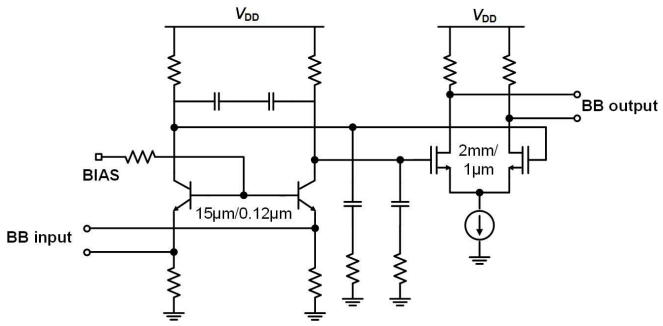

Fig. 10. Schematic of the baseband amplifiers.

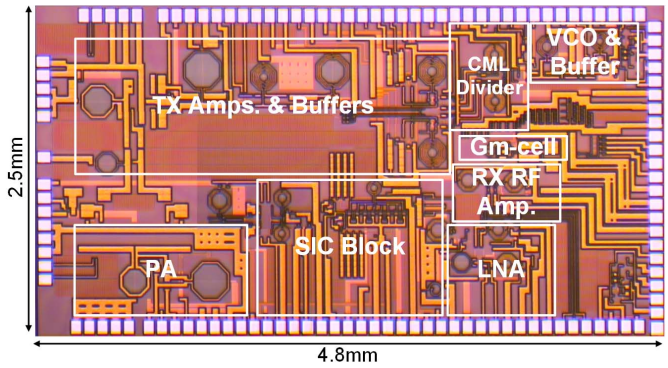

Fig. 11. Microphotograph of the fabricated chip.

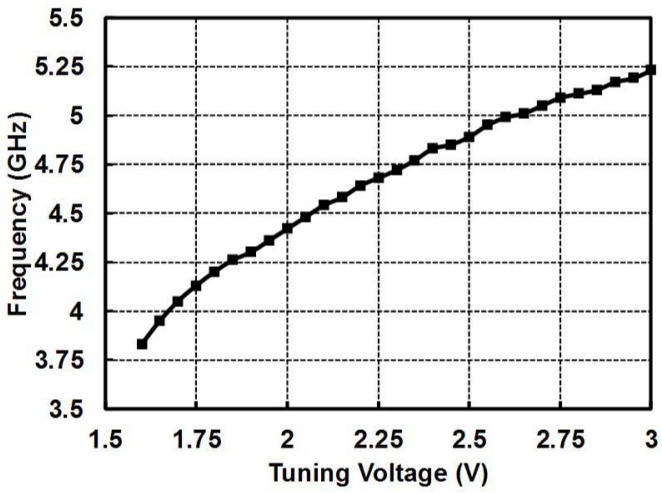

Fig. 12. Measurement results for the VCO tuning range.

determine if the cancellation circuit can cancel the TX self-interference signal across a wide range of phases, amplitudes, and frequencies. During this measurement, the TX output is connected to the RX input through an external phase shifter and a variable-gain attenuator. Therefore, the phase and amplitude of the self-interference signal can be externally controlled and varied. Moreover, the frequency of the self-interference signal can be controlled by varying the oscillation frequency of the on-chip VCO. As the phases, amplitudes, and frequency of the TX self-interference signal are varied, the control voltage of the on-chip self-interference cancellation circuit is changed to cancel the self-interference signal. As a proof-of-concept design, in this work, the control voltages are manually tuned using an external voltage supply with a step voltage of 0.01 V. In future works, a microcontroller can be used to automatically search for and generate the optimal tuning settings for the cancellation circuit. The measurement results are presented in Fig. 14. Clearly, the TX self-interference signal can be cancelled by at least 32 dB across a wide range of phases, amplitudes, and frequencies.

The RX conversion gain and linearity are studied next in Fig. 15. As shown in this figure, the RX achieves a conversion gain of 46 dB. If the self-interference cancellation circuit is turned off, the self-interference P1dB is -20 dBm. However, when the self-interference cancellation circuit is turned on and the TX self-interference signal is cancelled, the self-interference P1dB increases to -8 dBm.

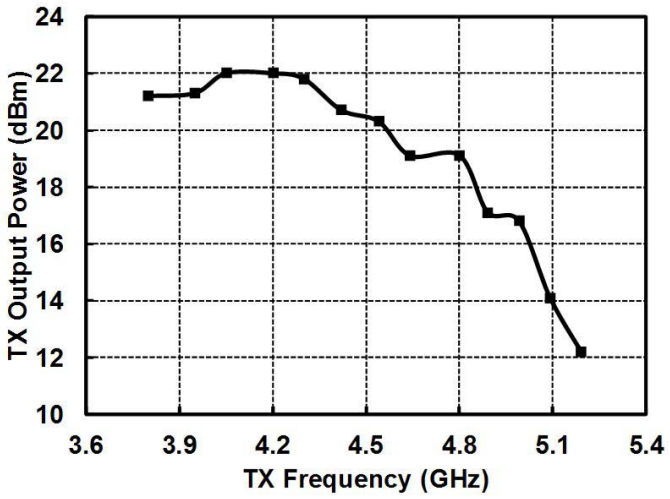

Fig. 13. Measured TX output power versus frequency.

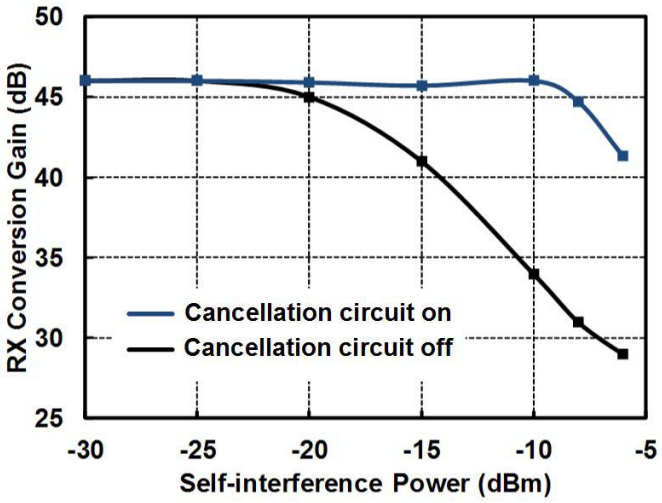

Fig. 15. Measurement results for the RX conversion gain.

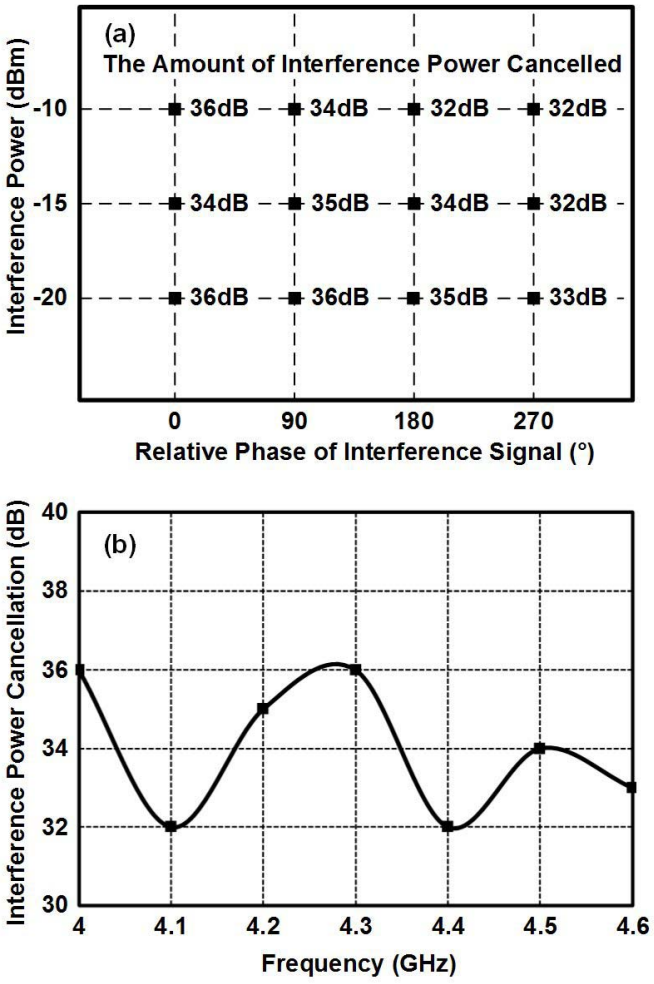

Fig. 14. (a) Measured self-interference cancellation under different interference power and phase. (b) Measured self-interference cancellation under different frequencies.

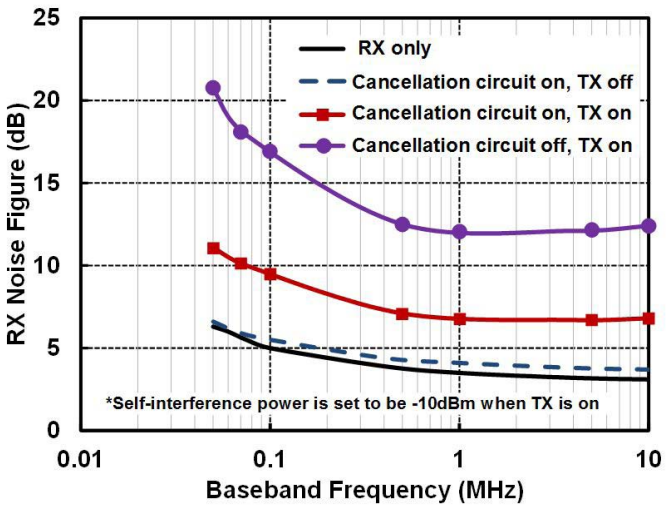

Fig. 16. Measurement results for the RX NF under various conditions.

This demonstrates the effectiveness of the self-interference cancellation circuit.

Finally, the NF of the RX is studied. During the NF measurement, a stable external RF source is used to generate the TX and LO signals for the down-conversion mixer. This improves measurement accuracy, especially at low baseband frequencies. As shown in Fig. 16, when both the TX and the cancellation circuit are turned off, the RX achieves a NF of 3.1 dB/6.3 dB at 10 MHz/50 kHz baseband frequencies. When the TX remains off and the cancellation circuit is turned on and configured at the maximum gain settings, the cancellation circuit incurs a noise penalty of no more than 0.6 dB across the baseband frequencies from 50 kHz to 10 MHz. When the TX and cancellation circuit are turned on and the self-interference power is -10 dBm at the RX input, the RX NF is 6.8 dB/11.1 dB at 10 MHz/50 kHz baseband. We believe that the degradation in the NF can be attributed to multiple factors, such as the increased noise of the power supply and ground rail caused by the TX. If the cancellation circuit is turned off under the same self-interference power, the RX NF is 12.4 dB/20.7 dB at 10 MHz/50 kHz baseband frequencies. This demonstrates that the self-interference cancellation circuit can improve the NF significantly when there is a strong TX self-interference signal at the RX input.

TABLE I
PERFORMANCE SUMMARY AND COMPARISON WITH PRIOR ARTS

	RFIC2014 [13]	ISSCC2015 [14]	ISSCC 2015 [15] + RFIC 2015 [16][1]	ISSCC2016	This work
Architecture	Noise-canceling LNA+ complex feedforward network	Current-mode mixer-first RX with frequency-domain RF equalization	Mixer-first RX with self-interference cancelling VM-downconverter	RX with integrated magnetic-free circulator+ interference cancellation	Self-interference cancellation at RF with large voltage gain before down-conversion
On-chip blocks	Transceiver	RX only	Transceiver[2]	RX only	Transceiver
Operating freq.	0.1-1.5GHz	0.8-1.4GHz	0.15-3.5GHz	0.6-0.8GHz	3.8-4.8 GHz
TX output power	-18dBm	N.A.	13dBm	N.A.	**22dBm**
Maximum RX gain	55dB	42dB	24dB	42dB	46dB
RX NF (TX & cancellation circuit Off)	5-8dB	4.8dB	6.3dB	5dB	**3.1dB**[3]
RX NF at 50kHz baseband frequency (TX & cancellation circuit Off)	N.A.	N.A.	N.A.	N.A.	**6.3dB**
RX 1/f noise corner (TX & cancellation circuit Off)	N.A.	N.A.	2MHz	N.A.	**60kHz**
RX NF degradation when cancellation circuit is on (TX Off)	N.A.	0.9-1.5dB	4-6dB	6.5dB	**<0.6dB**
RX NF when co-integrated TX is On and self-interference cancellation circuit cancels TX self-interference	10.5dB (-18dBm TX and self-interference power)	N.A.	N.A.	**N**.A.	**6.8dB/11.1dB at 10MHz/50kHz baseband frequency (22dBm/-10dBm TX/self-interference power)**
Self-interference P1dB	-17.3dBm	-8dBm	>+1.5dBm	-4dBm[4]	-8dBm
Technology	65nm CMOS	65nm CMOS	65nm CMOS	65nm CMOS	0.13µm BiCMOS
Area	1.5mm^2	4.8mm^2	2mm^2	1.4mm^2	12mm^2
Power consumption	43-56mW	63-251mW	152-185mW	100mW	2W
Supply voltage	1.2/2.5V	1.2/1.5V	1.2/2V	1.2/1.3/2.2V	1.5/2/2.5V

1. The RX and TX was reported in [15] and [16], respectively.
2. External inductor choke was used in the TX.
3. None of the other works reported the baseband frequency where the NF is measured. For fair comparison, we use the NF at 10MHz baseband frequency for our RX.
4. The signal power at the TX port of the circulator.

Table I compares the reported transceiver with prior in-band full-duplex transceivers. The reported transceiver achieves the lowest NF, especially at low baseband frequencies. The flicker noise corner of the reported transceiver is 60 kHz, more than one order of magnitude lower than prior works. Furthermore, the reported transceiver is the first work that demonstrates the operation of the in-band full-duplex RX and the associated self-interference cancellation circuit when a co-integrated TX is operating at the same time and frequency band and generating > 20 dBm power.

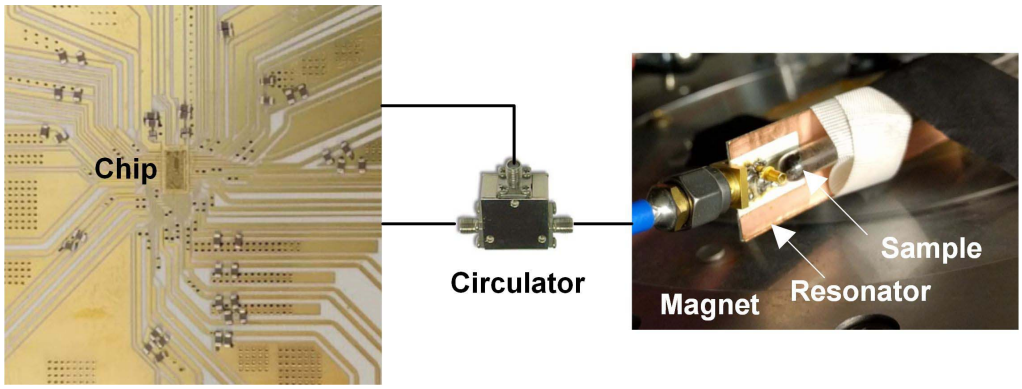

Fig. 17. Picture of the spectrometer setup.

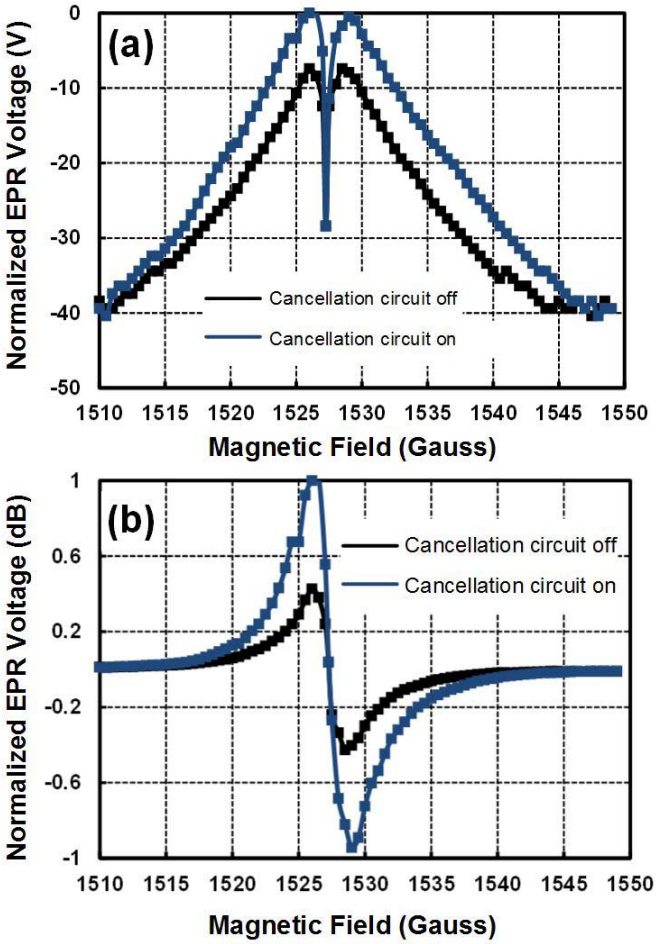

Fig. 18. Measured EPR response from DPPH powder sample in (a) log and (b) linear scale.

B. EPR Spectrometer Measurement Results

Utilizing the reported transceiver, an EPR spectrometer is built and tested, the picture of which is shown in Fig. 17. The resonator of the spectrometer has a quality factor of approximately 30. Its design details can be found in our earlier publication [11]. Fig. 18 plots the measured EPR response of a DPPH sample, using the assembled spectrometer. During the measurement, the frequency of the TX signal is fixed, and the B_0 field is swept with a 100 kHz modulation. The TX delivers around 20 dBm output power, and the self-interference power at the input of the RX is approximately -10 dBm. As shown in Fig. 18, if the cancellation circuit is configured to cancel the TX self-interference, the resulted SNR increases by approximately 7 dB. This demonstrates the effectiveness of the self-interference cancellation circuit. Compared to the previously reported EPR spectrometer based on a single-chip transceiver, the reported spectrometer shows 25 dB higher SNR by measuring the same sample [11].

V. Conclusion

In this paper, we report an in-band full-duplex transceiver for EPR spectroscopy application. The transceiver utilizes a self-interference cancellation circuit to mitigate the TX self-interference problem. In this work, the TX can deliver 20 dBm power while maintaining a low NF of RX under a strong TX self-interference signal. The transceiver has the lowest NF and flicker noise corner, compared to prior in-band full-duplex transceivers. Using the reported transceiver, an EPR spectrometer is built and tested. Compared to previous EPR spectrometers based on single-chip transceivers, the reported EPR spectrometer improves the SNR by 25 dB.

References

[1] J. A. Weil and J. R. Bolton, *Electron Paramagnetic Resonance: Elementary Theory and Practical Applications*. New York, NY, USA: Wiley, 2006.

[2] S. S. Velan, R. G. S. Spencer, J. L. Zweier, and P. Kuppusamy, "Electron paramagnetic resonance oxygen mapping (EPROM): Direct visualization of oxygen concentration in tissue," *Magn. Reson. Med.*, vol. 43, no. 6, pp. 804–809, Jun. 2000.

[3] J. Jiang, T. Nakashima, K. J. Liu, F. Goda, T. Shima, and H. M. Swartz, "Measurement of PO2 in liver using EPR oximetry," *J. Appl. Physiol.*, vol. 80, no. 2, pp. 552–558, 1996.

[4] J. Matsumoto *et al.*, "Absolute oxygen tension (pO2) in murine fatty and muscle tissue as determined by EPR," *Magn. Reson. Med.*, vol. 54, no. 6, pp. 1530–1535, Dec. 2005.

[5] L. Montanari, M. Clericuzio, G. Del Piero, and R. Scotti, "Asphaltene radicals and their interaction with molecular oxygen: An EPR probe of their molecular characteristics and tendency to aggregate," *Appl. Magn. Reson.*, vol. 14, no. 1, pp. 81–100, Feb. 1998.

[6] M. A. Volodin, G. V. Mamin, V. V. Izotov, and S. B. Orlinskii, "High-frequency EPR study of crude oils," *J. Phys., Conf. Ser.*, vol. 478, pp. 1–4, 2013.

[7] Y.-H. Lee and J. W. Corbett, "EPR studies of defects in electron-irradiated silicon: A triplet state of vacancy-oxygen complexes," *Phys. Rev. B*, vol. 13, pp. 2653–2666, Mar. 1976.
[8] J. Isoya, T. Umeda, N. Mizuochi, N. T. Son, E. Janzén, and T. Ohshima, "EPR identification of intrinsic defects in SiC," *Phys. Status Solidi B*, vol. 245, no. 7, pp. 1298–1314, Jul. 2008.
[9] J. Anders, A. Angerhofer, and G. Boero, "K-band single-chip electron spin resonance detector," *J. Magn. Reson.*, vol. 217, pp. 19–26, Aug. 2012.
[10] T. Yalcin and G. Boero, "Single-chip detector for electron spin resonance spectroscopy," *Rev. Sci. Instrum.*, vol. 79, no. 9, p. 094105, 2008.
[11] X. Yang and A. Babakhani, "A single-chip electron paramagnetic resonance transceiver in 0.13-μm SiGe BiCMOS," *IEEE Trans. Microw. Theory Techn.*, vol. 63, no. 11, pp. 3727–3735, Nov. 2015.
[12] C. P. Poole, Jr., and H. A. Farach, Eds., *Handbook of Electron Spin Resonance*, vol. 2. New York, NY, USA: Springer, 1999.
[13] D. Yang and A. Molnar, "A widely tunable active duplexing transceiver with same-channel concurrent RX/TX and 30 dB RX/TX isolation," in *Proc. IEEE Radio Freq. Integr. Circuits Symp.*, Jun. 2014, pp. 321–324.
[14] J. Zhou, T.-H. Chuang, T. Dinc, and H. Krishnaswamy, "Receiver with $>$20 MHz bandwidth self-interference cancellation suitable for FDD, co-existence and full-duplex applications," in *IEEE ISSCC Dig. Tech. Papers*, Feb. 2015, pp. 342–343.
[15] D.-J. van den Broek, E. A. M. Klumperink, and B. Nauta, "A self-interference-cancelling receiver for in-band full-duplex wireless with low distortion under cancellation of strong TX leakage," in *IEEE ISSCC Dig. Tech. Papers*, Feb. 2015, pp. 344–345.
[16] D.-J. van den Broek, E. A. M. Klumperink, and B. Nauta, "A self-interference cancelling front-end for in-band full-duplex wireless and its phase noise performance," in *Proc. IEEE Radio Freq. Integr. Circuits Symp.*, May 2015, pp. 75–78.
[17] J. Zhou, N. Reiskarimian, and H. Krishnaswamy, "Receiver with integrated magnetic-free N-path-filter-based non-reciprocal circulator and baseband self-interference cancellation for full-duplex wireless," in *IEEE ISSCC Dig. Tech. Papers*, Jan./Feb. 2016, pp. 178–180.
[18] B. Sanyal, S. P. Chawla, and A. Sharma, "An improved method to identify irradiated rice by EPR spectroscopy and thermoluminescence measurements," *Food Chem.*, vol. 116, no. 2, pp. 526–534, Sep. 2009.
[19] S. Zhou and M. C. F. Chang, "A CMOS passive mixer with low flicker noise for low-power direct-conversion receiver," *IEEE J. Solid-State Circuits*, vol. 40, no. 5, pp. 1084–1093, May 2005.
[20] A. Mirzaei, H. Darabi, J. C. Leete, and Y. Chang, "Analysis and optimization of direct-conversion receivers with 25% duty-cycle current-driven passive mixers," *IEEE Trans. Circuits Syst. I, Reg. Papers*, vol. 57, no. 9, pp. 2353–2366, Sep. 2010.
[21] D. Murphy *et al.*, "A blocker-tolerant, noise-cancelling receiver suitable for wideband wireless applications," *IEEE J. Solid-State Circuits*, vol. 47, no. 12, pp. 2943–2963, Dec. 2012.
[22] Bruker Corporation Model ELEXSYS-II E560. [Online]. Available: https://www.bruker.com

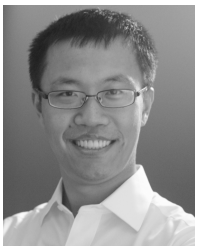

Xuebei Yang received the B.S. degree in microelectronics from Tsinghua University, Beijing, China, in 2008, and the M.S. and Ph.D. degrees in electrical and computer engineering from Rice University, Houston, TX, USA, in 2010 and 2016, respectively.

He is currently a Senior Analog IC Design Engineer at Oracle Corporation.

Dr. Yang was the recipient of the IEEE Microwave Theory and Techhiques Society (IEEE MTT-S) Graduate Fellowship for medical applications and the Chinese Government National Award for Outstanding Self-financed Students Abroad, both in 2015.

Aydin Babakhani received the B.S. degree in electrical engineering from Sharif University of Technology, Tehran, Iran, in 2003, and the M.S. and Ph.D. degrees in electrical engineering from the California Institute of Technology (Caltech), Pasadena, CA, USA, in 2005 and 2008, respectively.

He was a postdoctoral scholar at Caltech in 2009 and a research scientist at IBM T. J. Watson Research Center in 2010. He is currently an Assistant Professor in the Electrical and Computer Engineering Department and the Director of the Rice Integrated Systems and Circuits Laboratory at Rice University, Houston, TX, USA.

Dr. Babakhani has won multiple best paper awards including the Best Paper Award in IEEE RWS Symposium in 2016, the Best Paper Award in IEEE RWS Symposium in 2015, the Best Paper Award in IEEE IMS Symposium in 2014, and the 2nd Place Best Paper Award in IEEE IMS Symposium in 2016 and IEEE AP-S Symposium on Antennas and Propagation in 2016. He has more than 70 publications in peer-reviewed journals and conferences as well as 20 patents that are issued or pending. He received a prestigious NSF CAREER award in 2015, an innovation award from Northrop Grumman in 2014, and a DARPA Young Faculty Award (YFA) in 2012. He is a co-founder of MicroSilicon Inc. He received the Caltech Electrical Engineering Department's Charles Wilts Best Ph.D. Thesis Prize for his work on Near-Field Direct Antenna Modulation (NFDAM). From 2006 to 2008 he was the Vice Chair of the IEEE Microwave Theory and Techniques Society Metro LA/SFV Joint Sections MTT-S Chapter 17.1. He was the recipient of the Microwave Graduate Fellowship in 2007, the Grand Prize in the Stanford-Berkeley-Caltech Innovators Challenge in 2006, Analog Devices Inc. Outstanding Student Designer Award in 2005, as well as Caltech Special Institute Fellowship and Atwood Fellowship in 2003. He was also the Gold Medal winner of the National Physics Competition in 1998, and the Gold Medal winner of the 30th International Physics Olympiad in 1999, in Padova, Italy.